A Multi-Foci Metalens with Polarization-Rotated Focal Points

Xiaofei Zang, Hongzhen Ding, Yuttana Intaravanne, Lin Chen, Yan Peng, Jingya Xie, Qinghong Ke, Alexey V. Balakin, Alexander P. Shkurinov, Xianzhong Chen, Yiming Zhu,* and Songlin Zhuang*

Benefiting from the unprecedented capability of metasurfaces in the manipulation of light propagation, metalenses can provide novel functions that are very challenging or impossible to achieve with conventional lenses. Here, an approach to realizing multi-foci metalenses is proposed and experimentally demonstrated with polarization-rotated focal points based on geometric metasurfaces. Multi-foci metalenses with various polarization rotation directions are developed using silicon pillars with spatially variant orientations. The focusing characteristic and longitudinal polarization-dependent imaging capability are demonstrated upon the illumination of a linearly polarized light beam. The uniqueness of this multi-foci metalens with polarization-rotated focal points may open a new avenue for imaging, sensing, and information processing.

1. Introduction

Optical metasurfaces, 2D counterparts of metamaterials, have provided unprecedented capabilities in the modification of light wavefront, enabling a plethora of novel applications such as generalized Snell's law of refraction,[1–4] light beam shaping,[5–8] Spin-Hall effects,[9–12] holograms,[13–19] polarization control and analysis,[20–23] and nonlinear dynamics.[24–27] In comparison with traditional bulk lenses that rely on the required gradual phase change accomplished by controlling surface profile of the optical material, metalenses are ultrathin and ultraflat, which is desirable for device miniaturization and system integration. As fundamental optical elements, metalenses[28–33] have shown promising applications in imaging, lithography, spectroscopy, and laser fabrication due to the ultrathin configuration and ease of fabrication. In addition, metalenses can provide novel functions that are very challenging or impossible to achieve with conventional lenses, which can extend the imaging capability of the current optical systems. Benefiting from the exotic properties of metasurfaces, various types of metalenses with unusual functionalities have been developed. Examples include dual-polarity plasmonic metalens,[34] broadband/multispectral achromatic metalens,[35–38] metalens array,[39] light-sword lens,[40] multi-foci lens,[41] multifunctional metalens,[42] and polarization-dependent metalens.[43] An optical element with polarization manipulation functionality, that is, polarization rotator, has been used in many research areas ranging from optical isolators[44] to sophisticated organic structure analysis.[45] Thus far, the multi-foci metalens with polarization-controllable functionality has not been demonstrated yet. Unlike previously demonstrated multi-foci lenses,[41] we propose and demonstrate a multi-foci metalens with polarization-rotated functionality. Furthermore, although our novel metalens is realized based on the geometric metasurfaces, which are typically spin-dependent (only works for circularly polarized light beams), it can work for linearly polarized light. The approach is utilized to design terahertz (THz) multi-foci lenses with multiple polarization-rotated focal points. As a novel terahertz lens with unusual functionality, the longitudinal polarization-dependent imaging is experimentally demonstrated. The flexible and robust generation of the polarization-rotated multiple focal spots may find new applications such as polarization-dependent imaging, information detection, and displaying.

Prof. X. Zang, H. Ding, Prof. L. Chen, Prof. Y. Peng, Prof. J. Xie, Q. Ke, Prof. A. V. Balakin, Prof. A. P. Shkurinov, Prof. Y. Zhu, Prof. S. Zhuang
Terahertz Technology Innovation Research Institute, and Shanghai Key Lab of Modern Optical System
University of Shanghai for Science and Technology
No. 516 JunGong Road, Shanghai 200093, China
E-mail: ymzhu@usst.edu.cn

Y. Intaravanne, Dr. X. Chen
SUPA, Institute of Photonics and Quantum Sciences
School of Engineering and Physical Sciences
Heriot-Watt University
Edinburgh EH14 4AS, UK
E-mail: x.chen@hw.ac.uk

Prof. A. V. Balakin, Prof. A. P. Shkurinov
Department of Physics and International Laser Center
Lomonosov Moscow State University
Leninskie Gory 1, Moscow 19991, Russia

Prof. A. V. Balakin, Prof. A. P. Shkurinov
ILIT RAS – Branch of the FSRC "Crystallography and Photonics" of RAS
Svyatoozerskaya 1, 140700 Shatura, Moscow Region, Russia

The ORCID identification number(s) for the author(s) of this article can be found under https://doi.org/10.1002/lpor.201900182

DOI: 10.1002/lpor.201900182

2. Operating Principle

Figure 1 shows the schematic of a multi-foci metalens with polarization-rotated focal points. Upon the illumination of a linearly polarized THz beam, the metalens have two focal points, whose polarization directions are rotated in comparison with that

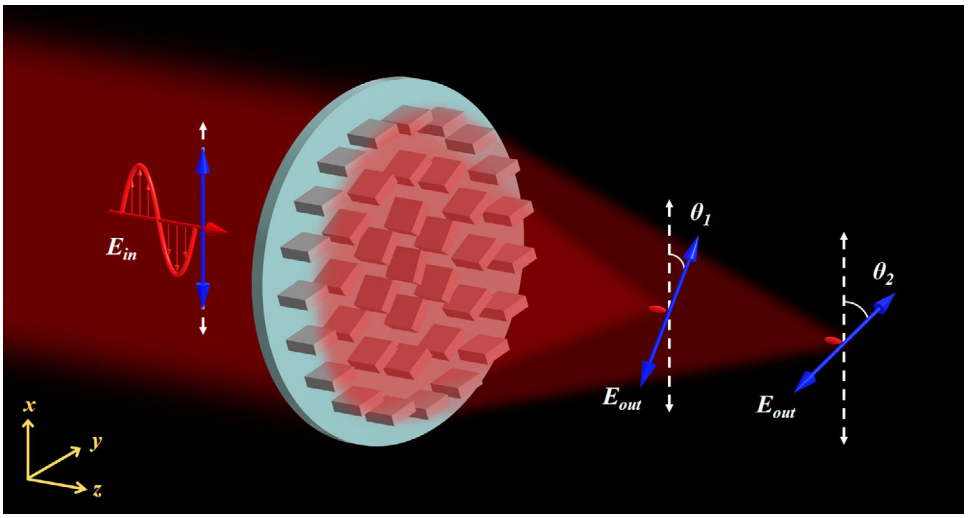

Figure 1. Schematic of the multi-foci metalens with polarization-rotated focal points. Under the illumination of linearly polarized THz waves, two longitudinally distributed focal spots. The polarization axis of the incident linearly polarized light beam is rotated at each focal point. The two polarization-rotated angles are θ_1 and θ_2, respectively.

of the incident light. Each focal spot with linear polarization can be considered as the superposition of both LCP and RCP components. Therefore, the key to realizing such multi-foci metalens mainly lies in the capability of a single metasuface to simultaneously focus linearly polarized incident beam and rotate the polarization direction of each focal spot. For simplicity, let us start with a metalens with a single polarization-rotated focal point, which will be extended multiple focal points later. To rotate polarization direction with an angle ϕ, the required transmitted THz fields can be written as

$$\frac{\sqrt{2}}{2}\left\{\frac{\sqrt{2}}{2}\begin{bmatrix}1\\ i\end{bmatrix}\exp\left(-i\phi\right)+\frac{\sqrt{2}}{2}\begin{bmatrix}1\\ -i\end{bmatrix}\exp\left(i\phi\right)\right\} \tag{1}$$

where the incident x-polarized THz beam can be considered as $\begin{bmatrix}1\\ 0\end{bmatrix}=\frac{\sqrt{2}}{2}\left\{\frac{\sqrt{2}}{2}\begin{bmatrix}1\\ i\end{bmatrix}+\frac{\sqrt{2}}{2}\begin{bmatrix}1\\ -i\end{bmatrix}\right\}$. To design a metalens without polarization-rotated functionality, the desired phase profile is governed by

$$\varphi(x,y)=\frac{2\pi}{\lambda}\left(\sqrt{x^2+y^2+f^2}-\left|f\right|\right) \tag{2}$$

in which λ is the working wavelength and f is the focal length. To combine the polarization rotation and focusing on the metalens, the corresponding Jones vector of transmitted beam can be expressed as follows.

$$\begin{aligned}&\tfrac{1}{\sqrt{2}}\left\{\tfrac{1}{\sqrt{2}}\begin{bmatrix}1\\ i\end{bmatrix}\exp\left(-i\phi\right)\exp\left(i\varphi(x,y)\right)\right.\\&\quad\left.+\tfrac{1}{\sqrt{2}}\begin{bmatrix}1\\ -i\end{bmatrix}\exp\left(i\phi\right)\exp\left(-i\varphi(x,y)\right)\right\}\\&+\tfrac{1}{\sqrt{2}}\left\{\tfrac{1}{\sqrt{2}}\begin{bmatrix}1\\ i\end{bmatrix}\exp\left(-i\phi\right)\exp\left(-i\varphi(x,y)\right)\right.\\&\quad\left.+\tfrac{1}{\sqrt{2}}\begin{bmatrix}1\\ -i\end{bmatrix}\exp\left(i\phi\right)\exp\left(i\varphi(x,y)\right)\right\}\end{aligned} \tag{3}$$

Since a linearly polarized light beam can be decomposed into LCP light beam and RCP light beam with same components, a metalens with polarization-rotated functionality can be achieved under the illumination of a linearly polarized THz beam.

The required phase distribution for metalens is governed by

$$\Phi(x,y)=\arg\left\{\exp\left[i\left(\phi+\varphi(x,y)\right)\right]+\exp\left[i\left(\phi-\varphi(x,y)\right)\right]\right\} \tag{4}$$

It should be noticed that the performance of metalens with the target phase profile shown in Equation (4) is implemented purely by geometric phase nanostructures. The target phase in Equation (4) consists of the phase profile of a convex lens (leading to focusing) and a concave lens (resulting in divergent beam). Therefore, under the illumination of LCP THz waves, only half of the transmitted waves will be converted to RCP light (for focusing) with an additional phase delay of ϕ. In contrast, for the RCP incidence, half of the transmitted waves will be converted to LCP light (for focusing) with an additional phase delay of $-\phi$. Under the illumination of linear-polarized light, a linear-polarized focal point with polarization-rotated functionality (with rotating angle of $\pm\phi$) can be realized. The rotation angle of $\pm\phi$ can be realized by rotating all nanostructures with an angle $\pm\phi/2$, resulting in the impart phase delays of $\pm\phi$ and $\mp\phi$ to RCP and LCP components, respectively. Here, only half of the transmitted THz waves converted to RCP/LCP light is attributed to the phase profile of a convex lens exp (φ) and a concave lens exp ($-\varphi$) in Equation (4). Therefore, for the linearly polarized incidence, the focusing efficiency cannot exceed 50% in theory.

Accordingly, the total phase requirement for a metalens with polarization-rotated focal spots (see schematic of Figure 1) can be described as.

$$\begin{aligned}\Phi_L(x,y)=\arg\{&\exp\left[i\left(\phi_1+\varphi_1(x,y)\right)\right]+\exp\left[i\left(\phi_1-\varphi_1(x,y)\right)\right]\\&+\exp\left[i\left(\phi_2+\varphi_2(x,y)\right)\right]+\exp\left[i\left(\phi_2-\varphi_2(x,y)\right)\right]\}\end{aligned} \tag{5}$$

where φ_1, φ_2 are the two phase profiles for the generation of two separate focal points, whose corresponding rotation angles of

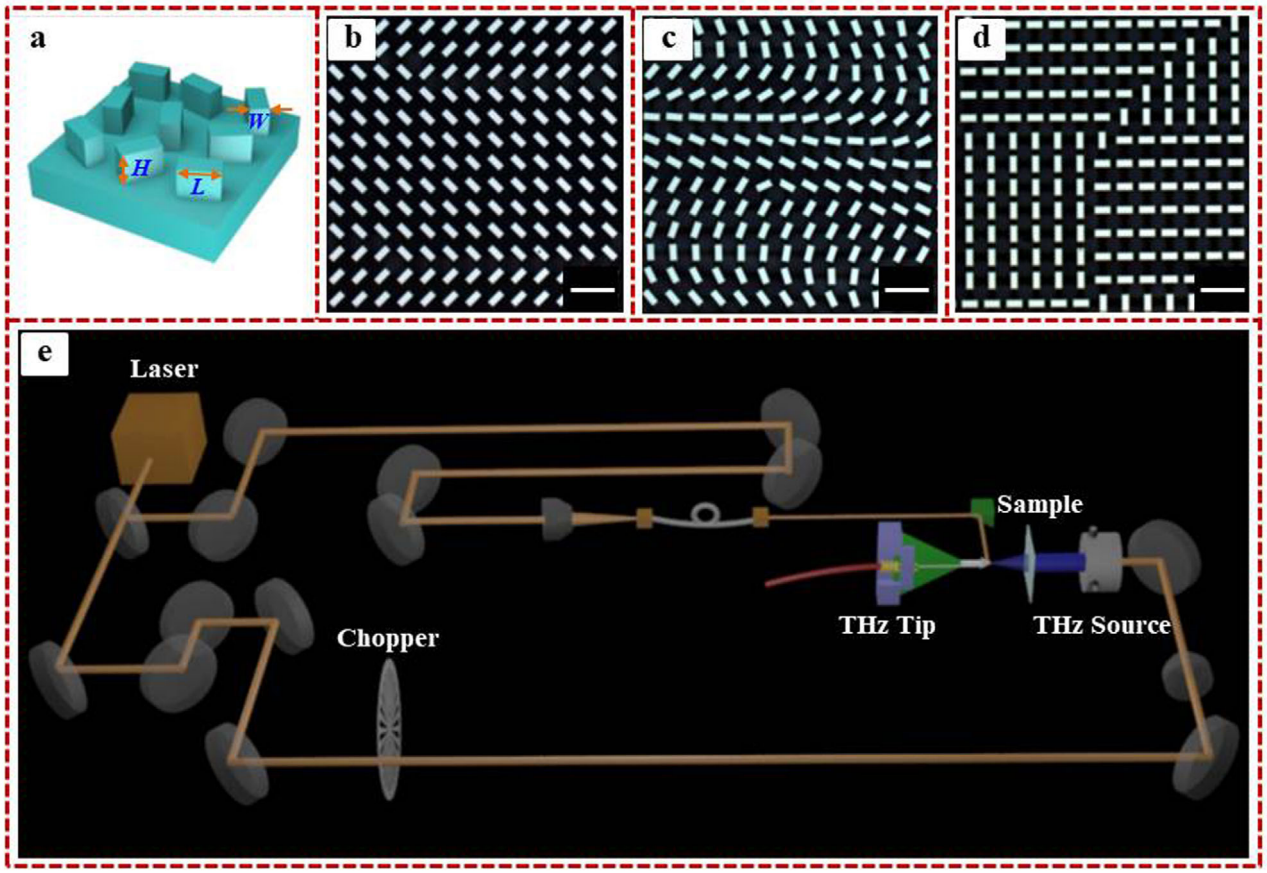

Figure 2. Design and fabrication of the metasurface and schematic of the experimental setup. a) Schematic of the designed metasurface with silicon-based micro-pillars sitting on a silicon substrate. b–d) The optical images of the fabricated metalenses to generate polarization-rotated single focal point, longitudinal multiple focal points, and transversal multiple focal points, respectively. The scale bar in the figures is 200 μm. e) Schematic of the experimental setup to characterize the properties of the metalens and polarization-dependent imaging. All of the designed metalenses consists of 100 × 100 micro-pillars, meaning that they are square, not circular. The side length of the square is 11.0 mm.

polarization are represented by ϕ_1 and ϕ_2, respectively. Although both φ_1 and φ_2 are designed based on Equation (2), the two focal lengths f_1 and f_2 are different. The rotation angles of these two longitudinally distributed focal spots can be the same ($\phi_1 = \phi_2 \neq 0$) or different ($\phi_1 \neq \phi_2$). As a consequence, the polarization rotation and focal lengths of the multi-foci metalens can be flexibly modulated with various combinations of ϕ_1, ϕ_2 and φ_1, φ_2. The design details of the proposed multi-foci metalens with polarization-rotated focal spots are given in Section 1, Supporting Information. The numerical simulation of polarization-independent focusing is provided in Section 2, Supporting Information.

3. Results

The dielectric metasurface consisting of anisotropic silicon micro-pillars with spatially variant orientations sitting on the silicon substrate is used to simultaneously realize lens focusing and polarization rotation, as shown in **Figure 2**a. Each micro-pillar in the metasurface can be considered as a half-wave plate, which can rotate the polarization or focusing by an abrupt phase (Pancharatnam–Berry phase) delay of $\pm 2\theta$, where θ is the angle between the long side of micro-pillar and x-axis, and the sign of the phase is determined by the helicity of the incident light beam (LCP or RCP). The length, width, and height of each micro-pillar are optimized as $L = 85$ μm, $W = 40$ μm, and $H = 500$ μm, respectively, and the pixel size is $P = 110$ μm along both x-axis and y-axis (the design of the silicon pillars is shown in Section 3, Supporting Information). Figure 2b–d shows the optical images of the fabricated metalens to generate single focal spot, longitudinal multiple focal spots, and transversal multiple focal spots, respectively. To characterize the performance of these unusual THz metalenses and polarization-dependent imaging, near-field scanning terahertz microscopy (NSTM) is utilized to detect the corresponding field distributions (see schematic of the experimental setup in Figure 2e). A laser beam with $\lambda = 780$ nm is splitted into two parts: one part of the beam is coupled onto the THz tip for detecting the field distributions, while the other part is shined on the photoconductive antenna to generate the THz waves. The THz tip is located in front of the sample to record the electric field distributions of focal points and imaging, while the position of the metalens is fixed. The measurement method is also shown in Section 6.

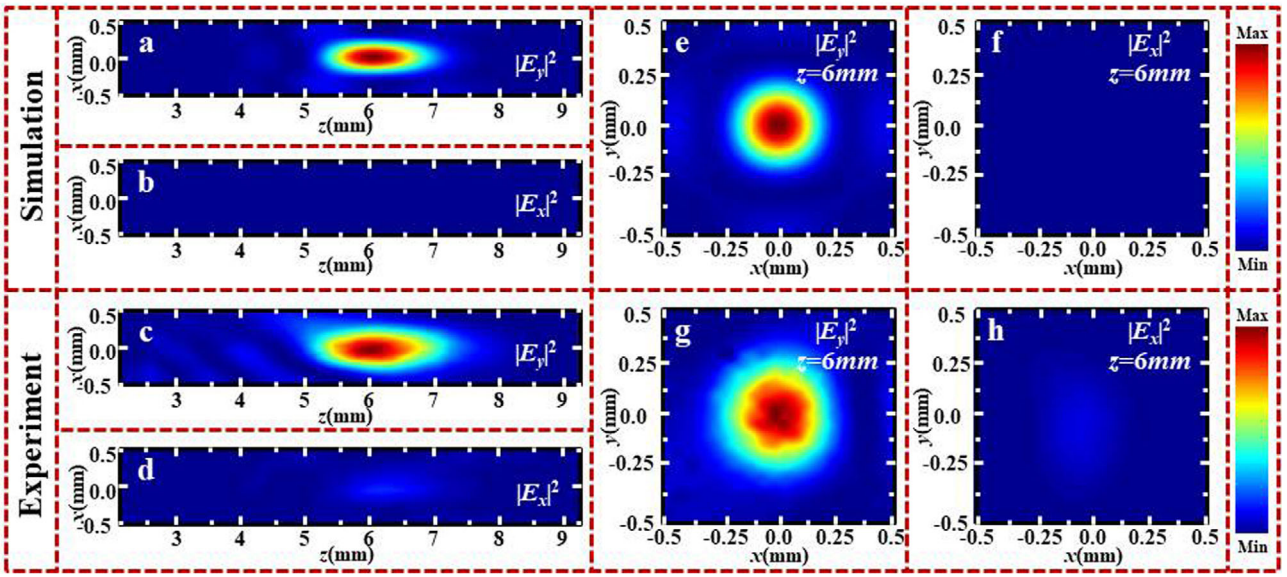

Figure 3. Electric field distributions for the metalens with a single polarization-rotated focal point. a,b) The simulated *y*- and *x*-polarized electric field distributions for the transmitted THz waves at *x*–*z* plane under the illumination of *x*-polarized THz waves. c,d) The corresponding experimental results. e,f) The simulated electric field distributions for the designed metalens at *x*–*y* plane and $z = 6$ mm. g,h) The corresponding measurements for the designed metalens at *x*–*y* plane and $z = 6$ mm.

As a feasibility study, a metalens with a single polarization-rotated focal point is initially demonstrated. Such a metalens (see Figure 2b) consists of 100 × 100 micro-pillars (with the corresponding side length of 11.0 mm), and the working frequency is 0.69 THz. The structure parameters in Equation (4) are as follows: $f = 6$ mm (focal length) and $\phi = 90$ (polarization rotating angle). **Figure 3** shows the numerical simulation and experimental results of this metalens. The finite difference time domain method is used to calculate the field distribution after the incident light passes through such metalens at normal incidence. For a linearly polarized incident THz beam with polarization along *x*-axis (*x*-polarized), one focal spot is clearly observed at $z = 6$ mm away from the surface of metalens, as shown in Figure 3a. It should be noted that the polarization axis of the incident light is rotated by 90^0 at the focal point. The *x*-polarized electric field distribution ($|E_x|^2$) of such metalens is also calculated, as shown in Figure 3b. It can be seen that none of the *x*-polarized electric field contributes to the focal spot, unambiguously demonstrating the polarization rotation of the converted THz beam (focal spot). The numerical calculations agree well with the theoretical design parameters of $f = 6$ mm and $\phi = 90°$. The experimental results are shown in Figure 3c,d. A linearly polarized (LP) THz beam along the *x*-axis is focused into a focal spot away from the sample surface (nearby $z = 6$ mm), and the polarization axis is rotated by an angle of 90°, generating a *y*-polarized focal spot. Both the experimental results and numerical simulations agree well with each other, except for a slight discrepancy, which can be attributed to the sample imperfection and the limited number of micro-pillars in metalens. The electric field distributions in *x*–*y* plane ($|E_x|^2$ and $|E_y|^2$) are also given in Figure 3e–h. At the real focal plane $z = 6$ mm, a focal spot with polarization rotation of $\frac{\pi}{2}$ is observed, as shown in Figure 3e,g, respectively, while none of the *x*-polarized focal spot is observed (see Figure 3f,h). The schematic that represents the characteristic of such metalens and the corresponding electric field distributions in *y*–*z* plane are given in Section 4, Supporting Information.

Nevertheless, a single device with more functions, that is, multiple focal spots with functionality of polarization rotation (see **Figure 4**), is desirable for device miniaturization and system integration. Inspired by this, we further design a longitudinal polarization-rotatable multi-foci metalens (see schematic of Figure 4 and sample of Figure 2c). According to Equation (5), we design such a metalens with structure parameters of $f_1 = 3$ mm (focal length of the first focal spot), $f_2 = 6$ mm (focal length of the second focal spot), $\phi_1 = 90°$ (rotation angle of polarization for left focal spot), and $\phi_2 = 0°$ (non-polarization rotation for the right focal spot). Under the illumination of *x*-polarized THz waves at 0.69 THz, a focal spot located at $z = 3$ mm with polarization along *y*-axis is achieved, as shown in Figure 4a. In contrast, an *x*-polarized focal spot is observed at $z = 6$ mm (see Figure 4b). Figure 4c,d shows the measured results, in which there are also two linearly polarized focal spots with orthogonal polarizations at $z = 3$ mm and $z = 6$ mm, respectively. Good agreement between the experimental results and theoretical prediction is observed, confirming the properties of multiple focal spots and polarization rotation. Figure 4e–h shows the corresponding electric distributions in *x*–*y* plane. The 2D field distributions also demonstrate the above characteristics. The calculations and measurements of the field distributions in *y*–*z* and *x*–*y* planes are also supplied in Section 5, Supporting Information.

Our design principle can not only steer THz beam to form multiple focal spots in longitudinal direction, but also enable the ability to harness the THz waves in transverse direction, leading to the transversal multiple focal points (see the principle of transversal multiple focal spots given in Section 1, Supporting Information). **Figure 5**a shows the schematic of proposed

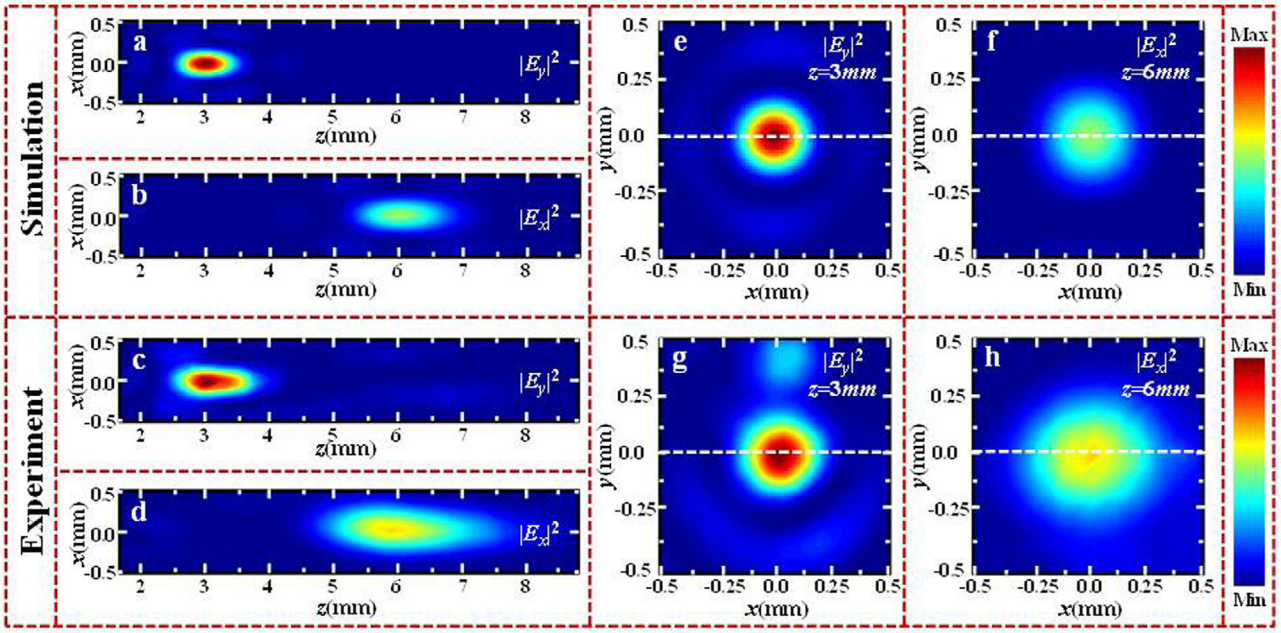

Figure 4. Electric field distributions for the metalens with polarization-rotated longitudinal multi-foci metalens. a,b) The simulated *y*- and *x*-polarized electric field distributions for the transmitted THz waves at *x*–*z* plane under the illumination of *x*-polarized THz waves. c,d) The corresponding measurements. e,f) The simulated electric field distributions for the designed metalens at *x*–*y* plane and $z = 3$ mm, $z = 6$ mm, respectively. g,h) The corresponding measurments for the designed metalens at *x*–*y* plane and $z = 3$ mm, $z = 6$ mm, respectively.

metalens that can split a linearly polarized THz beam into two LP focal spots in $\pm x$-axis without polarization rotation. The required phase distribution for such metalens is expressed as

$$\begin{aligned}\Phi_T(x,y) = \arg\{&\exp\left[i\left(\phi + \varphi(x,y) + \delta_x\right)\right] \\ &+ \exp\left[i\left(\phi + \varphi(x,y) - \delta_x\right)\right] + \exp\left[i\left(\phi - \varphi(x,y) + \delta_x\right)\right] \\ &+ \exp\left[i\left(\phi - \varphi(x,y) - \delta_x\right)\right]\}\end{aligned} \tag{6}$$

where $\delta_x = (\pi/7)$ is the phase gradient in *x*-axis, and the polarization rotating angle is 0 ($\phi = 0$, non-polarization rotation). Figure 5b,c shows the numerical results for the transversal multiple focal spots. Under the illumination of *x*-polarized THz waves, it is splitted and focused into two spots in transverse direction ($\pm x$-axis), and the polarization of each spot is parallel to the incident THz waves. The experimental demonstrations of beam splitters with functionality of focusing are given in Figure 5d,e, respectively. As illustrated in Figure 5f–i, the electric field distributions in *x*–*y* plane also reveal the function of our designed metalens. In addition, the transversal polarization-rotated multi-foci metalens is demonstrated in Section 6, Supporting Information.

4. Discussion

To simultaneously characterize the lens imaging functionality and polarization rotation capability, a polarization-dependent sample is designed, as shown in **Figure 6**a. As a proof-of-concept, we utilize longitudinal multi-foci metalens to realize THz polarization-dependent imaging. Although terahertz imaging[46,47] and tomography,[48] that are scanning imaging, have been successfully applied in the areas of nondestructive testing, such as pattern recognition and bio-imaging, the polarization-dependent imaging (for the polarization-dependent pattern) has not been demonstrated yet. Here, a Chinese character of "Sun" consisting of two symmetrically placed capital letters "E" is fabricated. Each capital letter is composed of periodic arranged metal slits coating on the PI (polyimide) film, in which the slit for the left "E" is parallel to *y*-axis while it is perpendicular to *y*-axis for the right "∃", as shown in Figure 6b. The numerical simulations of transmitting characteristics for the metal slit are shown in Section 7, Supporting Information. The calculations for polarization-dependent imaging are shown in Figure 6c,d. For the illumination of *y*-polarized THz waves, the left pattern of "E" is revealed, and the right "∃" is not observed (see Figure 6c). In this case, the incident THz waves is almost fully reflected on the left "E", and nearly perfectly transmitted on the right "∃" and surroundings, resulting in the pattern of "E". In contrast, for the *x*-polarized illumination, the right "∃" is observed. In our experiment, the location of the detector (THz tip) and metalens is fixed while the polarization-sensitive sample (embedded in the left or right focal spot) is scanning/shifting to reveal the desired pattern. As shown in Figure 6e,f, we observe two symmetrically placed capital letters "E" revealed from two polarization-orthogonal focal spots, demonstrating the properties of the multi-foci metalens with polarization-rotated focal points.

High temperature gas-cooled reactors (HTGRs), as the next generation nuclear plant (NGNP), are entirely dependent on the large graphite core.[49] Irradiation creep, a crucial property of nuclear graphite, is the tendency of graphite to deform permanently (or slowly move) due to the influence of radiation and temperature.[50] The irradiation creep of graphite may

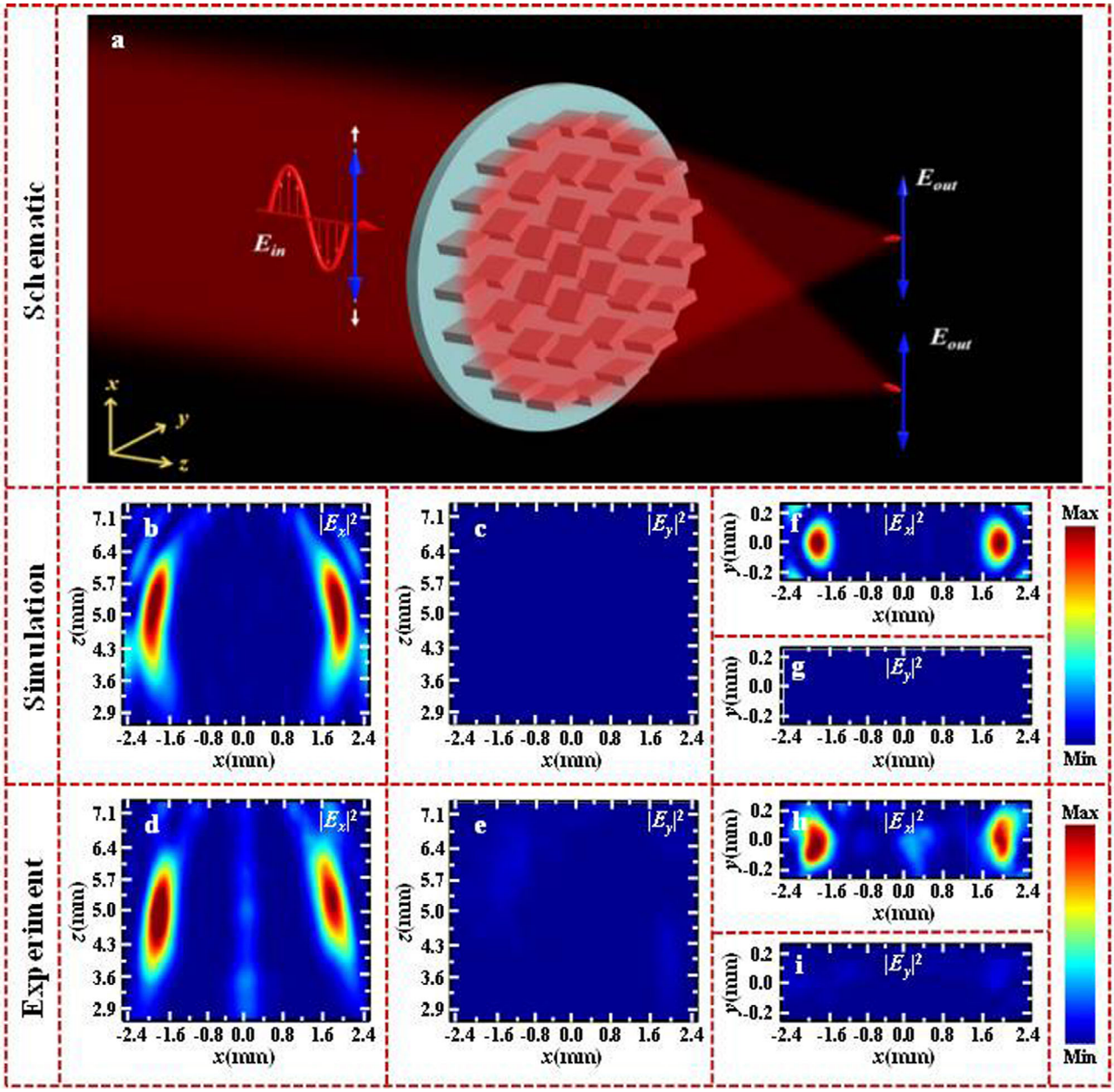

Figure 5. Schematic and electric field distributions for the transverse multi-foci metalens. a) The schematic for the transverse dual-foci metalens under the illumination of *x*-polarized THz waves. b,c) The simulated *x*- and *y*-polarized electric field distributions for the transmitted THz waves at *x*–*z* plane. d,e) The corresponding measurements for the metalens with polarization-rotated transverse dual-foci metalens. f,g) The simulated electric field distributions for the designed metalens at *x*–*y* plane and $z = 5$ mm, respectively. h,i) The corresponding measurments for the designed metalens at *x*–*y* plane and $z = 5$ mm, respectively.

become very large, and inevitably degrades its function under certain reactor conditions. Therefore, how to monitor the irradiation creep of graphite is critically important for HTGR. Terahertz polarization-dependent imaging of nuclear graphite is one of the most advanced approaches to detect the irradiation creep, since it is a nondestructive evaluation technique to monitor mechanical properties of graphite.[51] Our approach can be extended to design multiple focal spots (more than two focal points) with arbitrary polarization rotation directions. Therefore, it can be practically applied into the polarization-dependent imaging of nuclear graphite for detecting the irradiation creep of graphite.

Polarization conversion efficiency plays an important role in the evaluation of device performance. In this work, the polarization conversion efficiency is defined as the ratio between the power of desired polarization rotation and incident power, similar to that in ref. [52]. The polarization conversion efficiency for the micro-pillars with same orientations at 0.69 THz is 97% in the simulation. The detailed discussion of the simulated and measured polarization conversion efficiency and focusing

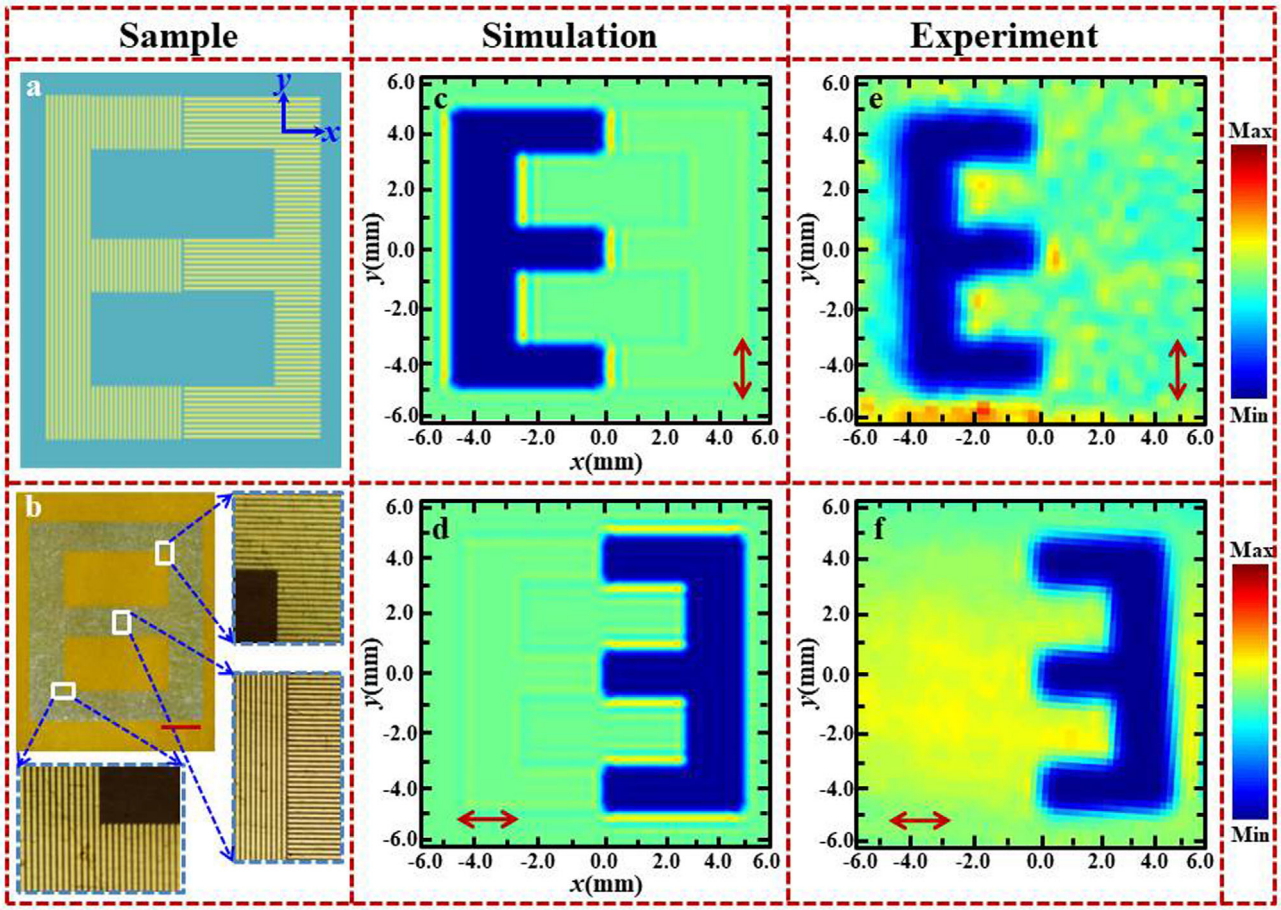

Figure 6. Polarization-dependent imaging. a,b) The schematic and optical image of the designed sample "Sun" for polarization-dependent imaging. c,d) The simulated electric field distributions for the designed imaging sample with the shinning of *x*- and *y*-polarized THz waves, respectively. e,f) The measured images with the designed imaging sample inside the left and right focal spots, respectively. Here, when the designed sample "Sun" is placed in the left spot, the left "E" can be revealed by scanning the sample (the sample is continuously moved while the THz tip is fixed to record the electric field distributions), while the right "∃" can be reconstructed by the right focal spot, resulting in the polarization-dependent imaging. The red scale bar in (b) is 2 mm.

efficiency (for simulations) are provided in Section 8, Supporting Information.

The approach can be used to design geometric metasurface with simultaneous control of the phase and polarization in all spatial dimensions, which can enable the capability to realize efficient functional THz multi-foci metalens with applications in polarization-dependent imaging. Inspired by device miniaturization and system integration, the longitudinal and transversal multi-focal metalens with functionality of polarization-manipulation are designed and experimentally demonstrated. In our work, the uniqueness of the proposed THz metalens is the integration of different functionalities, that is, longitudinal multiple focal spots with different polarizations, leading to the simultaneous multiplexing of focusing and polarization rotation in a single device. On the other hand, such polarization-rotated multi-foci metalens is directly applied for THz polarization-dependent imaging, which has not been demonstrated yet. Unlike the traditional metalens that were applied in diverse types of imaging such as magnified and demagnified imaging, achromatic imaging, and full-color light-field imaging, the polarization-dependent multi-foci metalens were designed for realizing multiple images that were revealed depending on the polarization. Our unique design will enable the metalens with unusual functions that are very difficult or impossible to achieve with conventional lenses.

5. Conclusion

In summary, we have proposed and demonstrated an approach to develop metalens with multiple polarization-rotated focal spots. The polarization axis of the incident linearly polarized light beam is rotated at each focal point. The longitudinal and transversal multiple focal spots with predesigned polarization rotation are experimentally demonstrated. Benefiting from unique property of the metalens, THz polarization-dependent imaging is demonstrated. The simplicity and robustness of our design not only provide a platform for simultaneous multiplexing of focusing and polarization rotation, but also open a novel avenue for polarization-dependent imaging.

6. Experimental Section

Sample Fabrication: We used a 1000-μm-thick intrinsic silicon wafer (<100>, Ω = 10 000 ohm) for the fabrication of the metalens. The AZP4620 photoresist (with thickness of 7–8 μm) was spun (with spin speed of 6000 RPM) onto the silicon wafers cleaned in ultrasonic bath. Then, the photoresist film was baked at 100 °C on a hotplate for 1 min. A mask aligner (IMP SF-100) was used for the exposure of the resist film. After the development process, the resist film with micro-pillars was baked at 100 °C for 2 min and then etched using the DRIE (Bosch) process with SF_6 and C_4F_8 for 95 min. Finally, the silicon micro-pillars were obtained after the photoresist is removed by using acetone. For the imaging sample, the photoresist was spin-coated on one side of the PI film, and the mask was utilized for exposure processing. The gold array (imaging sample) was formed after metal coating and ultrasonic stripping.

Experimental Setup: The near-field scanning terahertz microscopy (NSTM),[53,54] as illustrated in Figure 2e, was built up to perform the characterization of the fabricated samples. A femtosecond laser was used to generate a laser beam with a wavelength of 780 nm, which is splitted into two parts. One part of the light was guided into the photoconductive antenna emitter to generate THz waves, and the THz beam impinges on the metalens (and imaging sample). The other part was coupled into a single-mode fiber with a length of 10 cm, and then shined on the THz tip/detector for detecting the electric field distributions. The THz tip was mounted on a 3D translation stage, enabling the capability of 3D field scanning. The position of the metalens was fixed and the THz tip was inside the focusing region to scan the field distribution. The electric field was detected with a step size of 25 μm along both *x*-direction and *y*-direction and 100 μm step size along the *z*-direction. For the polarization-dependent imaging, the position of the metalens and THz tip was fixed while the imaging sample was moved step-by-step for imaging with a step size of 200 μm along both the *x*-direction and *y*-direction.

Supporting Information

Supporting Information is available from the Wiley Online Library or from the author.

Acknowledgements

X.Z., X.C., and Y.Z. initiated the idea. H.D. and X.Z. conducted the numerical simulations. H.D. and X.Z. performed the measurements. All authors prepared the manuscript. X.Z., X.C., and Y.Z. supervised the project. All the authors discussed and analyzed the results. This work is supported in part by the National Key Research and Development Program of China (2017YFA0701005), National Natural Science Foundation of China (61871268, 61722111), Natural Science Foundation of Shanghai (18ZR1425600), Shanghai Pujiang Program (18PJD033), "Shuguang" Program of Shanghai Education Commission (19SG44), Shanghai International Joint Laboratory Project (17590750300), and the 111 Project (D18014), Science and Technology Development Project of USST (2018KJFZ087), State Key Laboratory of Advanced Optical Communication Systems and Networks, Shanghai Jiao Tong University, China (2018GZKF03004). X.C. acknowledges the Engineering and Physical Sciences Research Council of the United Kingdom (Grant Ref: EP/P029892/1).

Conflict of Interest

The authors declare no conflict of interest.

Keywords

imaging, metalenses, metasurfaces, polarization control

Received: May 31, 2019
Revised: August 27, 2019

[1] N. F. Yu, P. Genevet, M. A. Kats, F. Aieta, J. P. Tetienne, F. Capasso, Z. Gaburro, *Science* **2011**, *334*, 333.
[2] L. Huang, X. Chen, H. Mühlenbernd, G. Li, B. Bai, Q. Tan, G. Jin, T. Zentgraf, S. Zhang, *Nano Lett.* **2012**, *12*, 5750.
[3] X. Ni, N. K. Emani, A. V. Kildishev, A. Boltasseva, V. M. Shalaev, *Science* **2012**, *335*, 427.
[4] X. Luo, *Sci. China: Phys., Mech. Astron.* **2012**, *58*, 594201.
[5] B. Walther, C. Helgert, C. Rockstuhl, F. Setzpfandt, F. Eilenberger, E. Kley, F. Lederer, A. Tunnermann, T. Pertsch, *Adv. Mater.* **2012**, *24*, 6300.
[6] X. Chen, Y.Zhang, L. Huang, S. Zhang, *Adv. Opt. Mater.* **2014**, *2*, 978.
[7] H. Liu, M. Mehmood, K. Huang, L. Ke, H. Ye, P. Genevet, M. Zhang, A. Danner, S. Yeo, C. Qiu, J. Teng, *Adv. Opt. Mater.* **2014**, *2*, 1193.
[8] X. Yin, Z. Ye, J. Rho, Y. Wang, X. Zhang, *Science* **2013**, *339*, 1405.
[9] M. Pu, X. Li, X. Ma, Y. Wang, Z. Zhao, C. Wang, C. Hu, P. Gao, C. Huang, H. Ren, X. Li, F.Qin, J. Yang, M. Gu, M. Hong, X. Luo, *Sci. Adv.* **2015**, *1*, e1500396.
[10] X. Ling, X.Zhou, X. Yi, W. Shu, Y.Liu, S. Chen, H. Luo, S.Wen, D. Fan, *Light Sci. Appl.* **2014**, *4*, e290.
[11] W. Luo, S. Xiao, Q. He, S. Sun, L. Zhou, *Adv. Opt. Mater.* **2015**, *3*, 1102.
[12] J. Zhou, H. Qian, G. Hu, H. Luo, S. Wen, Z. Liu, *ACS Nano* **2018**, *12*, 82.
[13] G. Zheng, H. Mühlenbernd, M. Kenney, G. Li, T. Zentgraf, S. Zhang, *Nat Nanotechnol.* **2015**, *10*, 308.
[14] Y. W. Huang, W. T. Chen, W. Tsai, P. Wu, C. Wang, G. Sun, D. P. Tsai, *Nano. Lett.* **2015**, *15*, 3122.
[15] D. Wen, D. F. Yue, G. Li, G. Zheng, K. Chan, S. Chen, M. Chen, K. F. Li, P. W. H. Wong, K. W. Cheah, E. Y. B. Pun, S. Zhang, X. Chen, *Nat. Commun.* **2015**, *6*, 8241.
[16] B. Wang, F. Dong, Q. T. Li, D. Yang, C. Sun, J. Chen, Z. Song, L. Xu, W. Chu, Y. F. Xiao, Q. Gong, Y. Li, *Nano. Lett.* **2016**, *16*, 5235.
[17] X. Li, L. Chen, Y. Li, X. Zhang, M. Pu, Z. Zhao, X. Ma, Y. Wang, M. Hong, X. Luo, *Sci. Adv.* **2016**, *2*, e1601102.
[18] L. Jin, Z. Dong, S. Mei, Y. Yu, Z. Wei, Z. Pan, S. Rezaei, X. Li, A. Kuznetsov, Y. Kivshar, J. Yang, C. Qiu, *Nano Lett.* **2018**, *18*, 8016.
[19] Y.Chen, J. Gao, X. Yang, *Light Sci. Appl.* **2018**, *7*, 84.
[20] N. K. Grady, J. E. Heyes, D. R. Chowdhury, Y. Zeng, M. T. Reiten, A. K. Azad, A. J. Taylor, D. A. R. Dalvit, H. T. Chen, *Science* **2013**, *340*, 1304.
[21] L. Cong, N.Xu, J. Gu, R.Singh, J. Han, W. Zhang, *Laser Photonics Rev.* **2014**, *8*, 626.
[22] R. Fan, Y. Zhou, X. Ren, R.Peng, S. Jiang, D. Xu, X. Xiong, X.Huang, M. Wang, *Adv. Mater.* **2015**, *27*, 1201.
[23] P. Wu, W. Tsai, W. Chen, Y. Huang, T. Chen, J. Chen, C. Liao, C. Chu, G. Sun, D. Tsai, *Nano Lett.* **2017**, *17*, 445.
[24] G. Li, S. Chen, N. Pholchai, B. Reineke, P. Won, E. Pun, K. Cheah, T. Zentgraf, S. Zhang, *Nat. Mater.* **2015**, *14*, 607.
[25] E. Almeida, G. Shalem, Y. Prior, *Nat. Commun.* **2016**, *7*, 10367.
[26] W. Ye, F. Zeuner, X. Li, B. Reineke, S. He, C. Qiu, J. Liu, Y. Wang, S. Zhang, T. Zentgraf, *Nat. Commun.* **2016**, *7*, 11930.
[27] F. Walter, G. Li, C. Meier, S. Zhang, T. Zentgraf, *Nano Lett.* **2017**, *17*, 3171.
[28] D. Hu, X. Wang, S. Feng, J. Ye, W. Sun, Q. Kan, P. Klar, Y. Zhang, *Adv. Opt. Mater.* **2013**, *1*, 186.
[29] D. Lin, P. Fan, E. Hasman, M. Brongersma, *Science* **2014**, *345*, 298.
[30] M. Khorasaninejad, W. Chen, R. Devlin, J. Oh, A. Zhu, F. Capasso, *Science* **2016**, *353*, 1190.
[31] M. Khorasaninejad, W. Chen, A. Zhu, R. Devlin, J. Oh, F. Capasso, *Nano Lett.* **2016**, *16*, 4595.

[32] B. Chen, P. Wu, V. Sun, Y. Lai, C. Chu, I. Lee, J. Chen, Y. Chen, Y. Lan, C. Huang, D. Tsai, *Nano Lett.* **2017**, *17*, 6345.
[33] C. Schlickriede, N. Waterman, B. Reineke, P. Georgi, G. Li, S. Zhang, T. Zentgraf, *Adv. Mater.* **2018**, *30*, 1703843.
[34] X. Chen, L. Huang, H. Mühlenbernd, G. Li, B. Bai, Q. Tan, G. Jin, C. Qiu, S. Zhang, T. Zentgraf, *Nat. Commun.* **2012**, *3*, 1198.
[35] A. Arbabi, Y. Horie, A. Ball, A. Faraon, *Nat. Commun.* **2015**, *6*, 7069.
[36] R. Panigua-Dominguez, Y. Yu, E. Khaidarov, S. Choi, V. Leong, R. Bakker, X. Liang, Y. Fu, V. Valuckas, L. Krivitsky, *Nano Lett.* **2018**, *18*, 2124.
[37] S. M. Wang, P. C. Wu, V.-C. Su, Y.-C. Lai, C. H. Chu, J.-W. Chen, S.-H. Lu, J. Chen, B. B. Xu, C.-H. Kuan, T. Li, S. N. Zhu,, D. P. Tsai, *Nat. Commun.* **2017**, *8*, 187.
[38] Z. Zhao, M. Pu, H. Gao, J. Jin, X. Li, X. Ma, Y. Wang, P.Gao, X. Luo, *Sci. Rep.* **2015**, *5*, 15781.
[39] R. Lin, V. Sun, S. Wang, M. Chen, T. Chung, Y.Chen, H. Kuo, J. Chen, J. Chen, Y. Huang, J. Wang, C. Chu, P. Wu, T. Li, Z. Wang, S. Zhu, D. Tsai, *Nat. Nanotechnol.* **2019**, *14*, 227.
[40] Z. Zhang, D. Wen, C. Zhang, M. Chen, W. Wang, S. Chen, X. Chen, *ACS Photonics*. **2018**, *5*, 1794.
[41] X. Chen, M. Chen, M. Mehmood, D. Wen, F. Yu, C. Qiu, S. Zhang, *Adv. Opt. Mater.* **2015**, *3*, 1201.
[42] D. Wen, F. Yue, M. Chen, X. Chen, *Sci. Rep.* **2016**, *6*, 27628.
[43] A. Arbabi, Y. Horie, M. Bagheri, A. Faraon, *Nat. Nanotechnol.* **2015**, *10*, 937.
[44] A. Shaltout, J. Liu, V. Shalaev, A. Kildishev, *Nano Lett.* **2014**, *14*, 4426.
[45] D. Kovtun, I. Kochikov, Y. Tarasov, *J. Mol. Struct.* **2015**, *100*, 311.
[46] M. Schirmer, M. Fujio, M. Minami, J. Miura, T. Araki, T. Yasui, *Bio. Opt. Express* **2010**, *1*, 354.
[47] J. Wang, R. Stantchev, Q. Sun, T. Chiu, A. Ahuja, E. Pickwell-MacPherson, *Bio. Opt. Express* **2018**, *9*, 6467.
[48] D. Suzuki, S. Oda, Y. Yawano, *Nat. Photonics* **2016**, *10*, 809.
[49] W. Windes, T. Burchell, M. Carroll, *Technical Report*, *Idaho National Laboratory*, **2010**.
[50] T. D. Burchell, *J. Nucl. Mater* **2008**, *381*, 46.
[51] J. Zhang, A. Redo-Sanchez, X. C. Zhang, presented at *Frontiers in Optics*, Rochester, NY, USA, October **2012**.
[52] X. Zang, F. Dong, F. Yue, C. Zhang, L. Xu, Z. Song, M. Chen, P. Chen, G. S. Buller, Y. Zhu, S. Zhuang, W. Chu, S. Zhang, X. Chen, *Adv. Mater.* **2018**, *30*, 1707499.
[53] L. Chen, Y. Wei, X. Zang, Y. Zhu, S. Zhuang, *Sci. Rep.* **2016**, *6*, 22027.
[54] L. Chen, D. Liao, X. Guo, J. Zhao, Y. Zhu, S. Zhuang, *Front. Inf. Technol. Electron. Eng.* **2019**, *20*, 591.